






RESEARCH ARTICLE | JANUARY 23 2024

Simulations of three-layer Richtmyer–Meshkov mixing in a shock tube

Special Collection: [Shock Waves](#)

James D. Sadler   ; Philip D. Powell  ; Mark Schalles; Carlton Louie; Jeffrey W. Jacobs  ; Ye Zhou 

 Check for updates

Physics of Fluids 36, 014120 (2024)

<https://doi.org/10.1063/5.0177419>



CrossMark



Physics of Fluids
 Special Topic:
 Flow and Civil Structures

Submit Today



Simulations of three-layer Richtmyer–Meshkov mixing in a shock tube

Cite as: Phys. Fluids **36**, 014120 (2024); doi: [10.1063/5.0177419](https://doi.org/10.1063/5.0177419)

Submitted: 21 September 2023 · Accepted: 17 November 2023 ·

Published Online: 23 January 2024



View Online



Export Citation



CrossMark

James D. Sadler,^{1,a)}  Philip D. Powell,¹  Mark Schalles,² Carlton Louie,² Jeffrey W. Jacobs,²  and Ye Zhou¹ 

AFFILIATIONS

¹Lawrence Livermore National Laboratory, 7000 East Avenue, Livermore, California 94550, USA

²Department of Aerospace and Mechanical Engineering, University of Arizona, Tucson, Arizona 85721, USA

Note: This paper is part of the special topic, Shock Waves.

^{a)} Author to whom correspondence should be addressed: sadler6@llnl.gov

ABSTRACT

The Richtmyer–Meshkov instability causes perturbations to grow after a shock traverses a fluid density interface. This increases the mixing rate between fluid from either side of the interface. We use the Flash Eulerian hydrodynamic code to investigate alterations when a thin third layer of intermediate density is placed along the interface, effectively creating two adjacent unstable interfaces. This is a common occurrence in engineering applications where a thin barrier initially separates two materials. We find that the width of the mixing layer is similar or slightly reduced; however, the total mass of mixed material can actually increase. The mixing layer becomes more compact and efficient. However, the normalized mixed mass decreases, meaning that finger entrainment becomes more important than in the simple two-layer case. The effect of adding the central layer appears to decrease when the Atwood number is decreased. The Flash results are also benchmarked against two-layer experimental data from a shock tube at the University of Arizona.

Published under an exclusive license by AIP Publishing. <https://doi.org/10.1063/5.0177419>

I. INTRODUCTION

When a shock wave passes the interface of fluids of disparate densities, mixing is induced via the Richtmyer–Meshkov instability (RMI).^{1,2} In a process closely related to the classical Rayleigh–Taylor instability in a gravitational field, the sudden acceleration imposed by the shock generates vorticity on the interface. This vorticity, in turn, causes any pre-existing perturbations to grow. If the perturbation amplitude is much less than its wavelength, the amplitude grows linearly with time. Eventually, once the perturbation amplitude has grown to be similar to its wavelength, the instability becomes nonlinear and its growth rate decreases.^{3–6} Simultaneously, the “fingers” of fluid stretching from the interface into each fluid begin to grow asymmetrically, with fingers of the denser material (known as spikes) obtaining an amplitude a_s that is greater than the amplitude a_b of the fingers of less dense material (known as bubbles). The subscript s refers to spike quantities, and the subscript b refers to bubble quantities.

If an incident shock passes from the lower density fluid (ρ_1) to the higher density fluid (ρ_2), the RMI will cause perturbations to grow from their initial shape. On the other hand, if the shock passes from the higher density fluid to the lower, perturbations will first decrease to zero before growing in the “negative” direction, such that the late time perturbation has a π phase shift relative to the initial condition.^{4,7} In

the instability’s (early) linear stage, the growth velocities approximately satisfy the relations

$$\frac{da_s}{dt} = \frac{da_b}{dt} = ka_0 A \Delta v, \quad (1)$$

where $k = 2\pi/\lambda$ is the perturbation wavenumber, λ is the perturbation wavelength, $a_0 = a_s(0) = a_b(0)$ is the initial perturbation amplitude, Δv is the velocity impulse imparted by the shock, and $A = (\rho_2 - \rho_1)/(\rho_2 + \rho_1)$ is the Atwood number.

The effectiveness of RMI-induced material mixing is a key question for many engineering applications, among them scram-jet engines. This is because combustion relies on effective mixing of the fuel with shocked air from the engine intake.^{8,9} In contrast, in nuclear fusion experiments, such as those at the National Ignition Facility, material mixing is a key degradation process that one seeks to avoid.^{10–12} Indeed, the reduction of instability-induced mixing of contaminants into the fusion fuel was a key contributor to the recent achievement of fusion ignition.¹³

The first objective of this work is to assess the accuracy of the Flash hydrodynamics simulation code in reproducing experimental RMI data from a gas shock tube at the University of Arizona.¹⁴ Comparisons are made to a system exhibiting two-fluid RMI, as

described above. Simulations are found to match well with the RMI growth rate and shape of the fluid flow data well into the nonlinear stage of instability growth.

One open question is how the presence of a thin third fluid layer, sandwiched between the two main layers, affects the shock-induced mixing. This is a question of relevance to several physics and engineering applications. Depending on the application, the density of this intermediate layer may be higher, lower, or in between the densities of the two main fluids. At one extreme, if the central layer is much thicker than the perturbation wavelength, there will be little interaction between the two interfaces and the problem reduces to two copies of two-fluid mixing. If, however, the intermediate layer has a thickness comparable to the perturbation wavelength, it will influence the perturbation growth of both interfaces into the nonlinear stage.^{15–17} In this situation, the ultimate impact of the intermediate layer on the mixing of the two main fluids is not obvious *a priori*. At sufficiently early times, the presence of the thin central layer will prevent mixing between the main fluids; at late times, the presence of two interfaces may even act to increase the mixing rate.¹⁸ However, if the central layer is of intermediate density, it will reduce the Atwood number at each interface (relative to the two-fluid case) and will thus reduce the mixing rate.¹⁹ The effect of the central layer is therefore not immediately obvious in the nonlinear stage and requires detailed numerical investigation.

The RMI of a single interface has been extensively investigated in experiments.^{20–22} The RMI instability of two interfaces has been recently investigated by Liang *et al.*^{23–27} Their experiments and simulations used a central intermediate density gas layer between two perturbed interfaces. Even in the linear stage, there were interesting modifications to the RMI. For example, in one case, the usual perturbation phase reversal for a heavy to light gas interface was not observed. To investigate the effect of two interfaces on the chaotic fluid mixing stage, our simulations in this work continue to much later times than those of Liang *et al.*^{26,28} Due to the lower effective Atwood number, we find that the perturbation growth is similar or reduced relative to the case of a single interface, while the total mixed mass often increases.

After benchmarking the Flash code against existing two-fluid experimental data in Sec. II, we then apply it to investigate the role of a third intermediate-density layer on shock-induced mixing in Sec. III.

II. FLASH CODE VALIDATION FOR RICHTMYER-MESHKOV FLOWS

The work of Morgan *et al.*¹⁴ established an experimental data set for low Mach number, two-dimensional, single-mode RMI growth well into the nonlinear stage, using an apparatus developed based upon that of an earlier study by Jacobs and Krivets.²⁹ In it, the RMI occurs in a shock tube filled with layers of ambient gases selected from helium (He), air (78% nitrogen, 21% oxygen, 1% other gases), carbon dioxide (CO₂), and sulfur hexafluoride (SF₆). At an ambient shock tube pressure of 0.93 Bar, the gas densities were 0.155, 1.14, 1.72, and 5.02 mg/cm³, respectively. Their equation of state is modeled as ideal and polytropic, with adiabatic indices 1.666, 1.4, 1.3, and 1.095, respectively. Given the different densities of these gases at ambient conditions, the interface between the layers was observed to be RMI unstable after the passage of a Mach 1.2 shock toward the denser side. A well-characterized repeatable initial perturbation was induced on the interface via shaking the shock tube. Diagnostics including high-

speed cameras took snapshots of the gas mass fractions and vorticity fields at late times.

The air to sulfur hexafluoride experimental results of Morgan *et al.*'s study were in moderately good quantitative agreement with fluid simulations using the Miranda and Ares codes.¹⁴ Minor differences arose from late-time interfacial accelerations due to fluid boundary layers in the experiment. We now compare the experimental results with simulations using a third numerical code called Flash, an Eulerian multi-physics hydrodynamics code³⁰ with adaptive grid refinement. We adopt two-dimensional Cartesian coordinates to solve the Euler equations (i.e., zero viscosity, diffusivity, and conductivity), using the HLLC Riemann solver and third-order interpolation. The domain size was $8.9 \times 267 \text{ cm}^2$.

The simulation was initialized with a two-fluid system (air and SF₆) with a perturbed interface in a shock tube, similar to the experimental design of Morgan *et al.*¹⁴ The air mole fraction profile was initialized to vary smoothly across the interface,

$$X_1(x, y) = \frac{1}{2} + \frac{1}{2} \operatorname{erf} \left[\frac{y - y_0 - a_0 \cos(kx)}{L} \right], \quad (2)$$

with the SF₆ mole fraction profile $X_2 = 1 - X_1$. In these expressions, y is the coordinate perpendicular to the interface, x is the coordinate along the interface, $y_0 = 0$ cm is the average initial interfacial position, $a_0 = 0.2$ cm is the initial perturbation amplitude, and $L = 0.20$ cm is the transition lengthscale measured on the experimental apparatus.³¹ The corresponding mass density profile was $\rho(x, y) = X_1 \rho_1 + X_2 \rho_2$, with species mass fractions $Y_1(x, y) = X_1 \rho_1 / \rho$ and $Y_2(x, y) = X_2 \rho_2 / \rho$. The air had mass density $\rho_1 = 1.14 \text{ mg/cm}^3$ and the SF₆ had mass density $\rho_2 = 5.02 \text{ mg/cm}^3$, giving a pre-shock Atwood number of 0.63.

The simulated evolution is then given by

$$\frac{\partial \rho Y_j}{\partial t} + \nabla \cdot (\rho Y_j \mathbf{u}) = 0, \quad (3)$$

$$\frac{\partial \mathbf{u}}{\partial t} + \mathbf{u} \cdot \nabla \mathbf{u} = - \frac{\nabla p}{\rho}, \quad (4)$$

$$\frac{\partial U}{\partial t} + \nabla \cdot [(U + p) \mathbf{u}] = 0, \quad (5)$$

$$U = \frac{1}{2} \rho |\mathbf{u}|^2 + \frac{p}{\gamma - 1}, \quad (6)$$

where \mathbf{u} is the fluid velocity, p is the scalar pressure, and U is the total fluid energy density. The local adiabatic index $\gamma(t, x, y)$ is calculated locally from the species mass fractions in the mixture and the adiabatic indices γ_j for each species.

Domain boundaries in x were reflecting, while the upper y boundary at $y = 87$ cm had a fluid inflow/outflow condition and the lower y boundary at $y = -180$ cm had a reflecting condition. Cell sizes varied adaptively between 0.014 and 0.9 cm, depending on the density variation. The grid for the simulation grew to contain over 600 000 cells. In keeping with the experimental setup (the case with 2.5 wavelengths across the shock tube), the perturbation wavelength was set to $\lambda = 3.56$ cm, with amplitude $a_0 = 0.2$ cm. The air species used adiabatic index 1.4 and the SF₆ species used adiabatic index 1.095. A shock was initialized by varying the density, pressure, and vertical velocity of the air above $y_s = 15$ cm in accordance with the

Rankine–Hugoniot conditions for shock Mach number 1.2 and adiabatic index 1.4. The simulation was performed for a duration of 15 ms.

Figure 1 compares the simulated mass fraction evolution to experimental observations¹⁴ in 1.5 ms increments. Overall, the comparison is favorable, most notably in the timing of (1) the emergence of mushroom cap vortices, and (2) the mushroom cap's detachment from the spike. Features such as the round shape of the mushroom cap and the fine ripples at its extremities are also consistent. The interfacial velocity $\Delta v \simeq 69.5$ m/s is within the quoted experimental range (65.92 – 70.45 m/s),¹⁴ and the initial growth rate $\dot{a}_0 \simeq 7.9$ m/s is also within the quoted experimental range (6.3 – 7.9 m/s). There are some boundary effects in the experiment that cause quite a different evolution of the left-most spike attached to the wall. Nevertheless, the height and shape evolution of the central spike and its mushroom cap is quite similar to that in the experiment.

A key distinction must be made between the entrainment of fluid fingers and the atomic-level material mixing. Although RMI and RTI cause penetration of fluid fingers through the interface, it is only microscopic diffusion processes that cause the materials to mix.³² Nevertheless, the growing fluid fingers can increase the mixing rate by increasing the surface area of the interface, especially in the nonlinear stage of the instability. In the simulations presented here, diffusion occurs through numerical cell-level processes, rather than an explicit physical model.

The most common measure of entrainment and mixing is given by the width of the mixing layer. One definition uses the highest position where all cells at that height have $Y_2 > 0.5$, and the highest position where any cell at that height has $Y_2 > 0.5$. The mixed width $W(t)$ is the distance between these two positions, and the amplitude $a(t)$ is typically taken as half of the mixed width.

Figure 2 shows both the absolute (a) and scaled (b) amplitude growth vs time. In order to establish a direct comparison with the experimental results of Fig. 8 in Ref. 14, the axes of (b) have been normalized using k and the initial growth velocity $\dot{a}_0 \simeq 7.9$ ms⁻¹, as taken from the simulations. As a test of grid independence, solid curves show the Flash results for various minimum cell sizes. Although the differences are slight, the better-resolved simulations are a closer match to results of the Miranda simulation documented in Ref. 14. The differences between the two Flash simulations with highest resolution are minor, meaning that the results are well converged with use of a grid resolution of 0.14 mm.

Early on, the simulated curves follow a trajectory close to that of the experimental data, the Miranda simulation and the Ares simulation. At late times, the experiment had acceleration that caused additional perturbation growth beyond the trajectory in the simulations. The additional acceleration is caused by the interaction of the flow with the shock tube walls, which creates boundary layers and mass flux across the contact discontinuity. The presence of acceleration was confirmed with isolated experiments in the shock tube.¹⁴ The Ares numerical simulations used a no-slip boundary condition,¹⁴ as opposed to the periodic or reflecting transverse domain boundaries in the present study and the Miranda simulation. This is why the Ares results had closer agreement with the experiment.

Having assessed the mixed width and amplitude, it will also be helpful to consider the convergence of an alternative method for quantifying fluid mixing, namely atomic mix. In particular, the degree of local two-species mixing can be quantified³² via the mixed density,

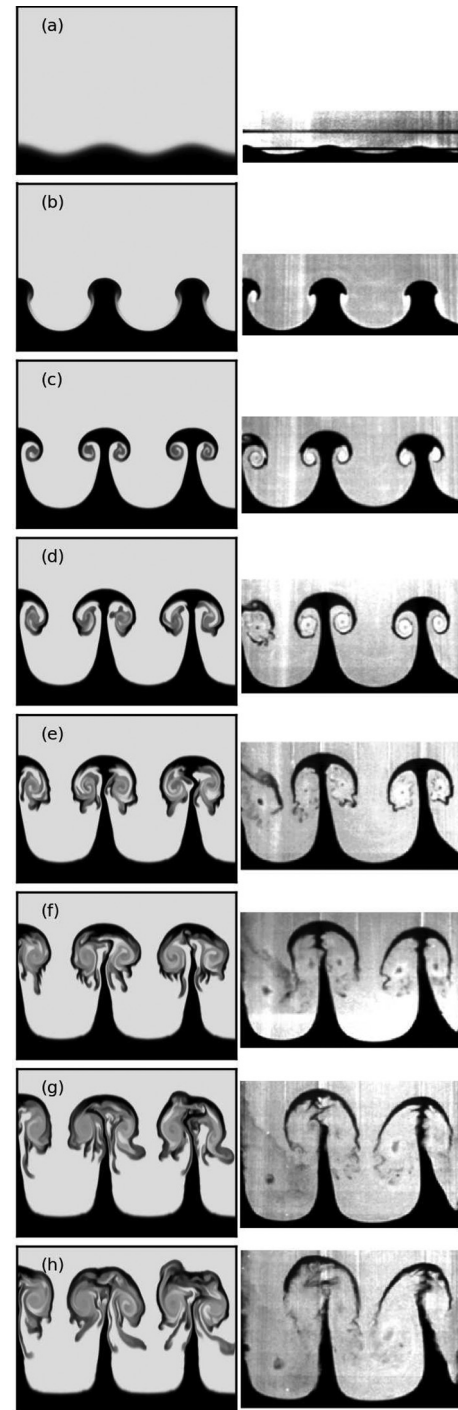


FIG. 1. Evolution of the SF₆ species mass fraction (darker regions) in the two-dimensional Flash simulation for air–SF₆. The panels are shown at times (a) 0, (b) 1.5, (c) 3, (d) 4.5, (e) 6, (f) 7.5, (g) 9, and (h) 10.5 ms. A moving portion of the full domain is shown. The corresponding images on the right are experimental Mie scattering snapshots on the same scale at the equivalent times.¹⁴ Note that the simulation data have been translated vertically so that the interfaces line up with those from the experiment. The reshock has not yet occurred in this figure.

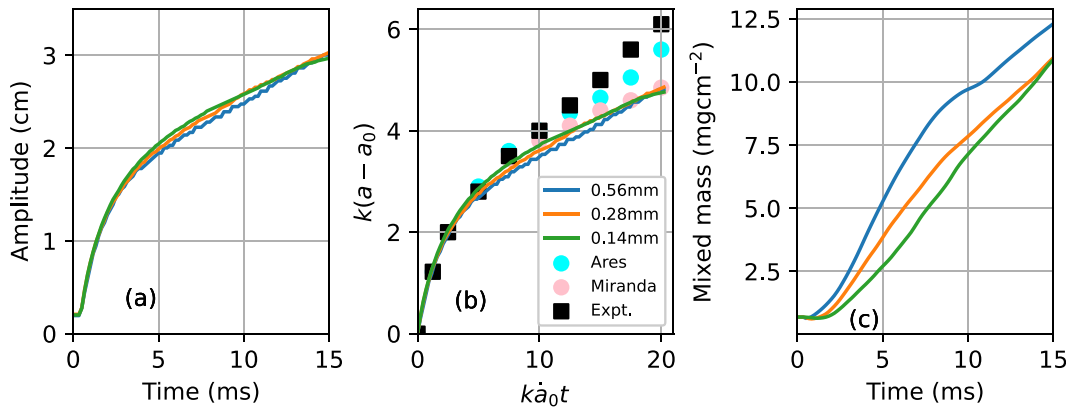


FIG. 2. Evolution of the perturbation amplitude ($a = W/2$) in the two-dimensional Flash simulation for air–SF₆ shown in Fig. 1. Results are shown for several simulations with different minimum cell sizes in the adaptive numerical grid. In panel (b), for a direct comparison to Fig. 8 in Ref. 14, the axes have been normalized using $k = 1.765 \text{ cm}^{-1}$ and the initial perturbation growth velocity $\dot{a}_0 = 790 \text{ cm/s}$. Squares indicate the experimental trajectory from Ref. 14 (shown in Fig. 1) and circles indicate the simulations in Ref. 14 using the Miranda and Ares codes. Panel (c) shows the mixed mass evolution for the three simulations with different minimal cell sizes.

$\rho_{12} = 4\rho Y_1 Y_2$, where Y_i is the i th species mass fraction and $\rho_{12} = \rho$ (i.e., $Y_1 = Y_2 = 1/2$) corresponds to a fully mixed region. The mixed mass, $M_{12} = \int \rho_{12} dV$, can be shown to be nondecreasing in time,³² and can only increase due to inter-species diffusion. As such, M_{12} is sensitive only to the amount of atomic mixing, and not to entrainment of fluid fingers. This gives it an advantage over the mixed width, which is sensitive to both atomic mixing and finger entrainment.

Figure 2(c) shows the mixed mass from the three simulations at different resolutions. Use of finer grid resolution decreases the mixed mass at later times. This is because the inter-species diffusion in the simulations occurs only due to numerical diffusion processes, which are sensitive to grid cell size. There is no explicit model of inter-species diffusion in these implicit large eddy simulations (ILES).³³ The artificial nature of small-scale diffusion processes is a drawback of the ILES approach, and it is unlikely to show grid convergence. Nevertheless, the differences in mixed mass for the two most-resolved simulations are minimal at late times. This acts as a verification that the simulations at the 0.14 mm resolution give sensible results for the mixed mass. As the amplitude in Fig. 2(a) is a metric dependent on large-scale features and the mixed mass in Fig. 2(c) is a metric integrating the mixing in small-scale features, these metrics give an independent validation of the numerical convergence at small and large scales.

III. THREE-LAYER MIXING

A. High Atwood number simulations

Having benchmarked the Flash code for two-layer RMI growth in a gas shock tube, we now proceed to investigate the three-layer case. Several three-fluid simulations were performed, using various combinations of the same four gases employed in the two-fluid simulations described above: He, air, CO₂, and SF₆. The gases were initialized to a pressure of 0.93 Bar.

The first case considered is helium–air–SF₆. A two-fluid control simulation was performed using He and SF₆, with a shock of Mach number of 1.1 initialized in helium. The interface at $y_0 = 0 \text{ cm}$ was perturbed via the mole fraction profile of Eq. (2), with $\lambda = 3.56$, $a_0 = 0.5$, and $L = 0.46 \text{ cm}$. Simulations were performed for a

duration of 15 ms. In a separate three-layer simulation with helium–air–SF₆, an intermediate layer of air with a thickness of 3 cm (on the order of the wavelength) was included, with the He/air interface located at $y_0 = 3 \text{ cm}$ and with $L = 0.63 \text{ cm}$. The perturbation was imposed only on the lower of the two interfaces. The x domain boundaries were at $x = 0$ and $x = 7.12 \text{ cm}$, with a periodic boundary condition, and the y boundaries were at $y = -110$ and $y = 68 \text{ cm}$. The numerical algorithms and resolution were the same as quoted in Sec. II.

Figure 3 shows the density evolution in the pair of simulations described above, with the top set of panels corresponding to the two-fluid case, while the bottom panels include the intermediate air layer, visible between $y = 0$ and $y = 3 \text{ cm}$. The shock transit occurs early in the simulation, around 0.1 ms, which induces a shock-compression of the SF₆. The perturbation grows quickly in both cases and reaches the deep nonlinear regime by the time the simulation is stopped. After 2 ms, the spike develops a mushroom cap through the action of the Kelvin–Helmholtz instability.³⁴ In both cases, the spike is transversely much thinner than the bubble. Vortices are shed from the spike tips, and fluid is mixed in small-scale structures. By the final panel ($t = 14 \text{ ms}$), the initial $\lambda = 3.56 \text{ cm}$ perturbation is barely discernible and the RMI has entered the chaotic mixing stage.⁴ One important complication is the shock’s reflection from the bottom of the domain, after which it travels upward, eventually transiting the interfaces a second time in the opposite direction. In the final two panels, this reshock compresses the mixing layer and significantly alters the fine scale flow structures.^{35–40} The reshock occurs at $t \approx 11 \text{ ms}$.

A further aspect that alters the RMI from the classical treatment is the nonzero initial transition width L , which causes a diffuse boundary between the materials. This will decrease the density gradient at the interfaces and thus decrease the baroclinic vorticity generation $\partial(\nabla \times \mathbf{u})/\partial t = \nabla \rho \times \nabla p/\rho^2$, which is proportional to the density gradient as the shock transits. It is known that this decreases the RMI growth, at least in the linear stage.⁴¹ The diffuse transition widths in our simulations were chosen based on the experimental measurements for each gas combination.³¹

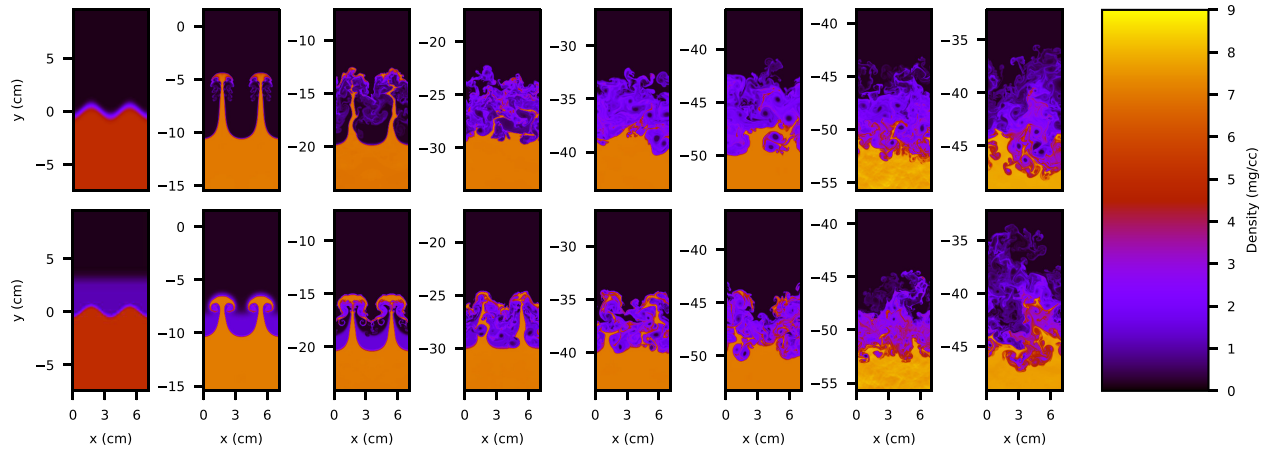


FIG. 3. Density evolution from two-dimensional Flash simulations of He-air-SF₆. Upper panels show the control two-fluid simulation (no central air layer), while lower panels show the simulation with a 3 cm air layer. Panels are separated by 2 ms along each row. The main shock transits downward after the first panel, and the reflected shock transits upward at $t = 11$ ms, before the second-to-last panel.

The initial evolution of the three-layer system is typical of lower Atwood number RMI. This is because the SF₆-air interface has $A = 0.63$, lower than the SF₆-He interface with $A = 0.94$. Growth initially occurs only at the lower interface, and the mushroom caps are more pronounced than in the control case. The spike tip breaks through to the upper interface at $t \simeq 2$ ms. At this point, mixing between helium and SF₆ begins. At all times, the mixed width is visibly smaller than in the control case.

Realistic perturbations in applications of interest are unlikely to be localized to just one of the two interfaces. Manufacturing defects or material grains will perturb the upper and lower interfaces. For example, a key perturbation in inertial confinement fusion is the fill tube, a micrometer-sized tube used to fill the target capsule with hydrogen fuel.⁴² Figure 4 shows two further simulations in which both interfaces were perturbed with amplitude $a_0 = 0.5$ cm and wavelength $\lambda = 3.56$ cm. The relative phase of the perturbations makes a significant

difference to the fluids' late-time evolution. When the perturbations are in-phase, the lower spike collides with the rear of the upper spike. This causes the upper spike to become detached after 2 ms, after which it merges with the lower spike. In the antiphase case, the upper spikes remain separated. Sensitivity to the phase of adjacent perturbations has previously been reported in numerical work.⁴³ Another interesting feature is the small low-density vortices that propagate downward into the SF₆. This behavior has been observed previously in simulations.⁴⁴⁻⁴⁷

Eventually, given a sufficiently high Reynolds number and simulation time, the fluid fingers may become turbulent across a broad range of length scales.^{48,49} This cascade of turbulent kinetic energy to small scales can rapidly increase material mixing.

Figure 5 shows the positions of the 99% and 1% mass fraction contours for Helium and SF₆ as functions of time. These are defined as the positions where $\langle Y_1 \rangle = 0.99$, $\langle Y_1 \rangle = 0.01$, $\langle Y_2 \rangle = 0.99$, and

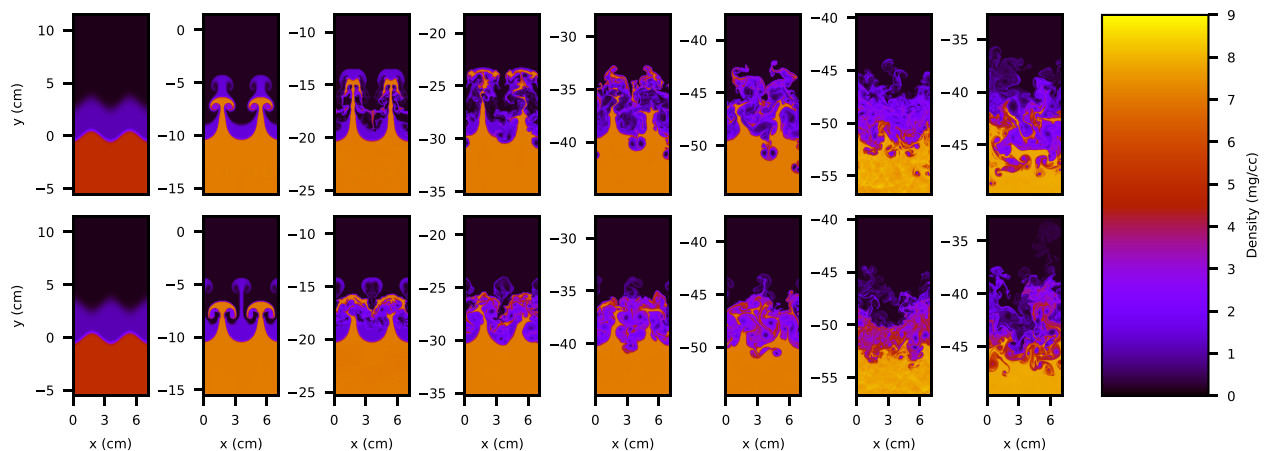


FIG. 4. Density evolution from two-dimensional Flash simulations of He-air-SF₆. Upper panels correspond to a 3 cm central air layer and both interfaces perturbed, while lower panels correspond to both interfaces perturbed in antiphase. Panels are separated by 2 ms along each row. The main shock transits downward after the first panel, and the reflected shock transits upward at $t = 11$ ms, before the second-to-last panel.

15 February 2024 19:57:20

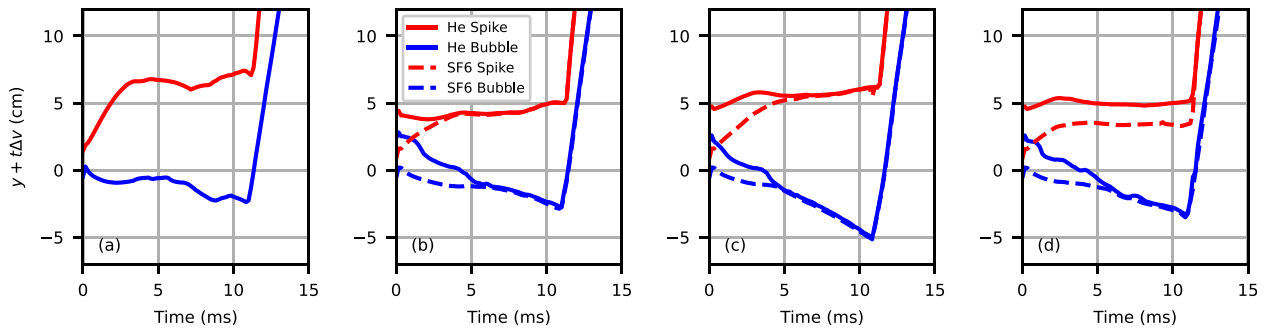


FIG. 5. Positions of the 99% species mass fractions in the two-dimensional Flash simulations shown in Figs. 3 and 4. Panels correspond to (a) the control case with no central air layer, (b) 3 cm air layer and perturbation only on the lower interface, (c) both interfaces perturbed in phase, and (d) both interfaces perturbed in antiphase. The upward reshock occurs at $t = 11$ ms.

$\langle Y_2 \rangle = 0.01$, where angled brackets indicate the transverse mean. The sudden acceleration imposed by the reshock is visible at $t \simeq 11$ ms. Panel (a) shows the control case, which quickly develops a mixing layer with growth that slows over time. Note that the initial gap between the lines at $t = 0$ is due to the initial 0.5 cm amplitude perturbation and the initial transition lengthscale L . In the three-layer case, shown in Fig. 5 (b), mixed layer growth is initially restricted to the lower interface (dashed lines), as only that interface was perturbed. After around 2 ms, however, the SF_6 perturbs the upper interface as well. This induces growth of the gap between the He 1% and 99% positions (solid lines). At late times, a complex mixing layer develops and the mixed width is similar, whether it is measured by helium or SF_6 . However, this is not true in the antiphase perturbation case. Here, the spike of air escapes from the main mixing layer and remains separate until the reshock arrives.

It is evident in Fig. 5 that the presence of an intermediate layer reduces the rate of spike growth, flattening the curves. The bubble growth is similar to the control case. This suggests that the addition of an intermediate layer preferentially affects the spikes, consistent with the interpretation of a lower effective Atwood number, as bubble-spike asymmetry typically increases with the Atwood number.⁵⁰

Figure 6(a) shows the mixed widths—defined as the distance between the 99% He mass fraction position and the 99% SF_6 mass fraction position—as functions of time. In the three-layer case, this definition implies an initial value of $kW \simeq 9$, arising from the 3 cm air layer thickness, the initial perturbation amplitude, and the diffuse mass fraction transition. The time axis has been normalized using the initial growth of the control case. The simulations in Fig. 3 are reflected in the blue and orange lines. It is evident that the presence of a central air layer reduces perturbation and mixed width growth. Even once the perturbation breaks through into the helium region (after $k\hat{a}_0t = 10$), its growth is lower than that of the control simulation (blue), an effect that may be attributed to the reduced Atwood numbers. Similarly, the reduced RMI can be viewed as arising from the fact that the intermediate density layer creates a density gradient perpendicular to the interface. The situation is then similar to the known suppression of RMI with a smooth density transition.⁵¹ The strong initial mixed width growth can be partly recovered if both interfaces are perturbed at $t = 0$ (green line). As expected, the mixed width's early evolution is independent of the relative phase of the interfacial perturbations. The reshock at $k\hat{a}_0t = 28$ compresses the mixing layer, before it rapidly expands at an even faster pace. This evolution of W is similar to that of previous

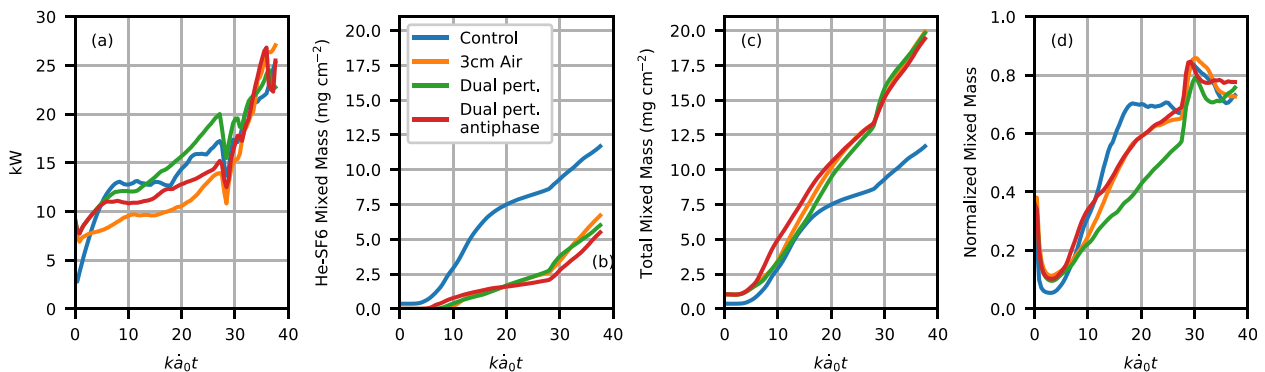


FIG. 6. Analysis of the two-dimensional Flash simulations for He–air– SF_6 shown in Figs. 3 and 4. (a) The mixed width, defined as the distance between the 99% He and 99% SF_6 mass fraction positions. Curves show the control case with no central air layer, the case with a 3 cm air layer and perturbation only on the lower interface, the case with both interfaces perturbed and the case with both interfaces perturbed in antiphase. (b) The mixed mass between the two outer layers of He and SF_6 . (c) The total mixed mass, which is the sum of the mixed masses between each of the three pairs of species. (d) The normalized total mixed mass, which gives an indication of the transverse homogeneity of the mixing layer.

experimental and simulation data.^{52–58} Afterward, the mixed widths are similar for each case.⁵⁹

When more than two material species are present, several mixed densities can be defined: two-species mixed densities, $\rho_{ij} = 4\rho Y_i Y_j$, and their corresponding mixed masses, $M_{ij} = \int \rho_{ij} dV$. Thus, in the three-layer system, we have M_{12} , M_{13} , and M_{23} . We can further define the sum of the two-material mixed densities, $\rho_{\text{tot}} = \rho_{12} + \rho_{13} + \rho_{23}$, and the total mixed mass $M_{\text{tot}} = M_{12} + M_{13} + M_{23}$. The total mixed mass provides a means for quantifying the total amount of fluid mixing as it is the sum of nondecreasing quantities, and is therefore itself a nondecreasing quantity.

Figure 6 shows the He–SF₆ mixed mass (M_{12}) and the total mixed mass M_{tot} as functions of time. Due to the nonzero initial transition width L , the two-fluid control case has nonzero initial M_{12} ; the three-layer cases, however, initially have separation between the He and SF₆, leading to $M_{12} \simeq 0$. The curves for M_{12} possess similar qualitative features as the mixed widths. The central air layer decreases the interaction between the He and SF₆ layers, and the He–SF₆ mixed mass is negligible until $k\hat{a}_0 t \simeq 8$, when the perturbation breaks through. The increased mixing rate caused by the reshock is also visible. Some insight into the total amount of mixing can be obtained by considering the total mixed mass, which provides a much more even picture—until late times there is little difference in the amount of total mixing in the four cases. However, in the chaotic mixing stage and reshock stage, the three-layer cases have a higher total mixed mass. Interestingly, despite all cases having similar mixed width after the reshock, the three-layer cases produce a much larger total mixed mass. This suggests that the three-layer case produces a more efficient mixing layer than the two-layer control case. Another notable point is that the mixed masses in the three-layer cases are more sensitive to the reshock.

A final quantity of interest is the normalized mixed mass,³²

$$\Psi = \frac{\int \rho(Y_1 Y_2 + Y_1 Y_3 + Y_2 Y_3) dV}{\int \langle \rho \rangle (\langle Y_1 \rangle \langle Y_2 \rangle + \langle Y_1 \rangle \langle Y_3 \rangle + \langle Y_2 \rangle \langle Y_3 \rangle) dV}. \quad (7)$$

This quantity is normalized to lie between zero and one. Its magnitude gives an idea of the transverse homogeneity of the mixing layer. After all, $\Psi = 1$ only when $\rho = \langle \rho \rangle$, $Y_1 = \langle Y_1 \rangle$, $Y_2 = \langle Y_2 \rangle$, and

$Y_3 = \langle Y_3 \rangle$. In other words, there is no dependence of any quantity on the transverse x coordinate. The upper limit $\Psi = 1$ indicates that the layer consists of atomically mixed mass, and the lower limit $\Psi = 0$ indicates interlocking fingers of separate species. The development of Ψ is in keeping with that found in previous work on two-layer RMI.³² Its initial value is nonzero due to the finite-width diffuse material transition. After the shock transit, the value rapidly drops as the bubbles and spikes penetrate through the interface. At later times, small-scale structures create atomic mixing and mixed mass, and so Ψ recovers to a larger value $\simeq 0.7$. It is interesting to note that the control case has the largest normalized mixed mass before the reshock, despite having the smallest absolute mixed mass of the four cases. This means that in the three-layer cases, the added interface increases the actual amount of mixed mass, but decreases the importance of the mixed mass relative to the spike and bubble entrainment. The case with double perturbations is exceptionally well affected, agreeing with the simple intuition that finger entrainment is relatively more important when there are more perturbations for the fingers to grow from.

Finally, after the reshock, all cases have a similar value of $\Psi \simeq 0.8$. This is because the reshock merges the two separate mixing layers into one, and a single well-advanced layer was previously found to asymptote at $\Psi \simeq 0.7 - 0.8$.³²

B. Low Atwood number simulations

We now turn to consider the problem of three-layer fluid mixing at a lower Atwood number. Figures 7 and 8 show simulations with the same setup, except the He–air–SF₆ layers have been replaced with air–CO₂–SF₆ layers. The transition scale length was $L = 0.2$ cm. The dimensions, shock Mach number, and other initialization parameters were identical to those of the simulations represented in Fig. 3. In agreement with the previous cases, the addition of the central layer at intermediate density slightly stalls the RMI development. Some bubble acceleration is visible just before the reshock in the control case.

Figure 9 shows the bubble and spike positions for the four cases described above. In the control case, the bubble acceleration begins at around $t = 10$ ms, leading to a much faster growth in the mixed width. The bubble acceleration is much smaller in the other cases,

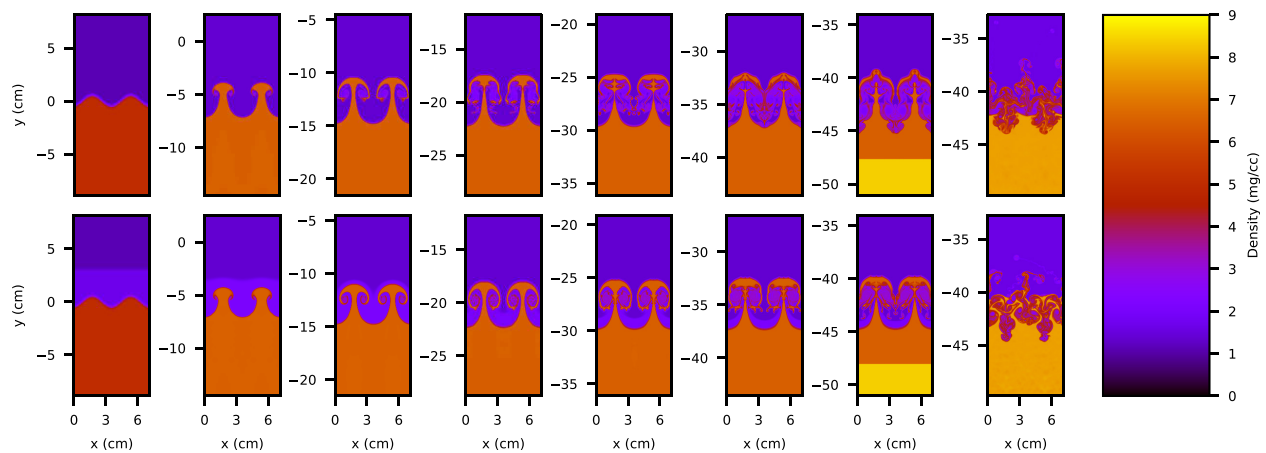


FIG. 7. Density evolution from the two-dimensional Flash simulations for air–CO₂–SF₆. Lower (upper) panels show the simulation with (without) a central 3 cm CO₂ layer. Panels are separated by 2 ms along each row. The approaching reshock is visible at $t = 12$ ms. Only a portion of the full domain is shown.

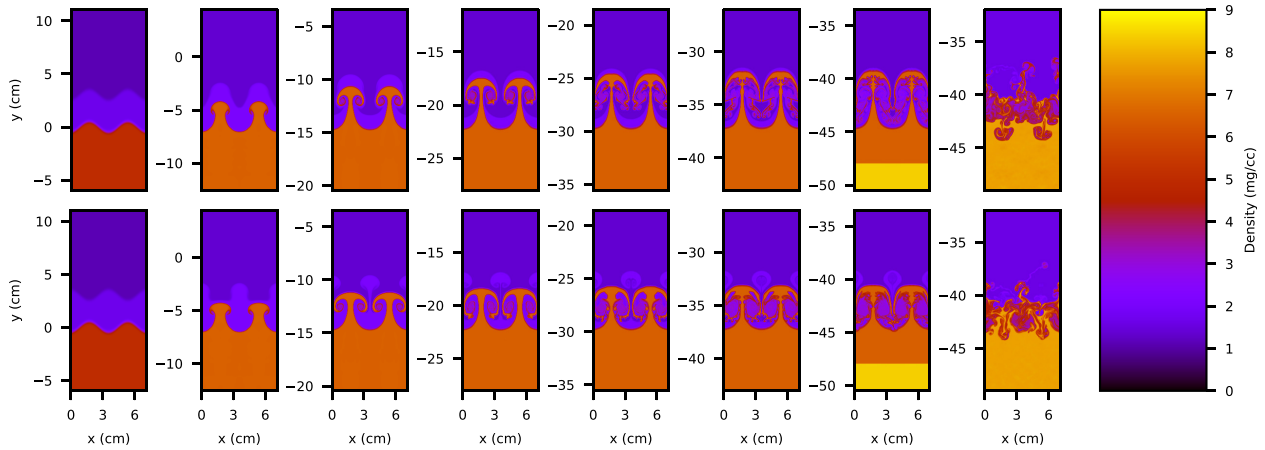


FIG. 8. Density evolution from two-dimensional Flash simulations for air-CO₂-SF₆. Upper panels show the simulation with both interfaces perturbed, and lower panels show the simulation with both interfaces perturbed in antiphase. Panels are separated by 2 ms along each row. The approaching reshock is visible at $t = 12$ ms.

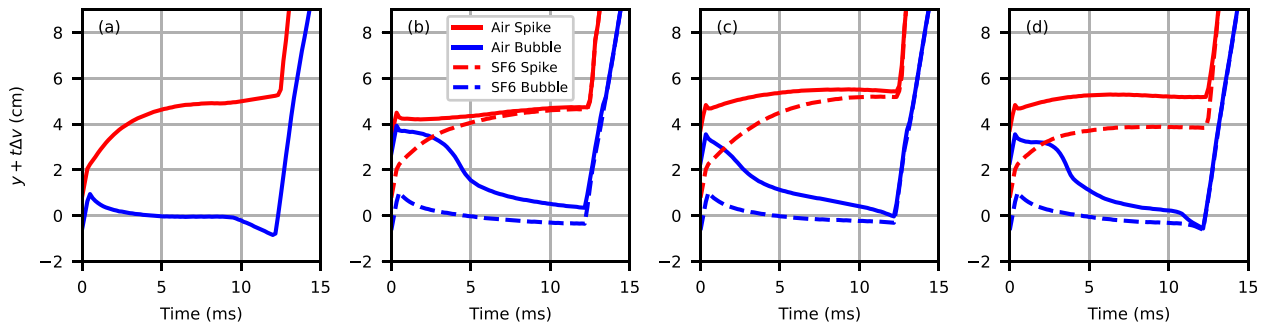


FIG. 9. Positions of the 99% mass fractions in two-dimensional Flash simulations for air-CO₂-SF₆ shown in Figs. 7 and 8. Panels show (a) the control case with no central CO₂ layer, (b) a 3 cm intermediate CO₂ layer with perturbation only on the lower interface, (c) both interfaces perturbed in-phase, and (d) both interfaces perturbed in antiphase.

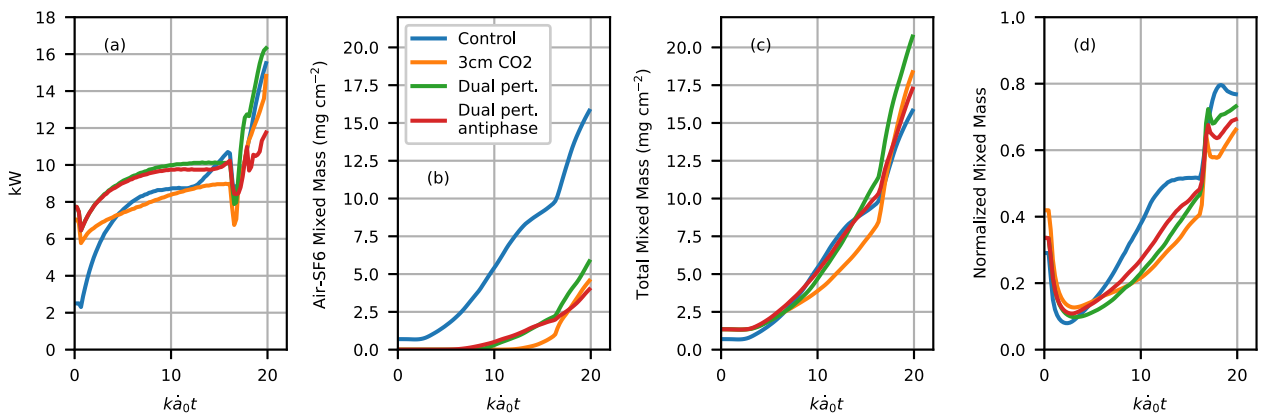


FIG. 10. Analysis of the two-dimensional Flash simulations for air-CO₂-SF₆ shown in Figs. 7 and 8. (a) The mixed width measured using the distance between the 99% air and 99% SF₆ mass fraction positions. Curves show the control case with no central CO₂ layer, the case with a 3 cm CO₂ layer and perturbation only on the lower interface, the case with both interfaces perturbed, and the case with both interfaces perturbed in antiphase. (b) The mixed mass between the two outer layers of air and SF₆. (c) The total mixed mass, which is the sum of the mixed masses between each of the three pairs of species. (d) The normalized total mixed mass, which gives an indication of the transverse homogeneity of the mixing layer.

suggesting that the central layer suppresses or delays the bubble acceleration. In agreement with Fig. 5, the bubbles and spikes for each species begin to merge at late times, leaving only a single discernible mixing layer. Again, the antiphase case creates a spike of the central layer that remains detached until the reshock transits at $t = 12$ ms.

Figure 10(a) shows the mixed widths for the cases described above. Adding the central layer slightly reduces the mixed width just before the reshock. Adding the dual perturbation causes an increase. This is in agreement with the He-air-SF₆ simulations discussed previously. The antiphase perturbation has a much lower mixed width after the reshock. The effect of the central layer on the mixed width is less pronounced than for the high Atwood number simulations, and all four cases have a similar mixed width at the time the reshock arrives.

The mixed masses are shown in Figs. 10(b) and 10(c). As observed at a high Atwood number, the central layer greatly reduces the mixed mass M_{12} growth. The reshock causes a sudden increase in the mixed mass growth rate, and the in-phase perturbation case has the highest total mixed mass. In contrast to Fig. 6, the total mixed masses are fairly similar for each case. This shows that the effects of adding a third layer are more pronounced at a higher Atwood number.

The normalized mixed masses are shown in Fig. 10(d). Again, the three-layer cases have a decreased value of Ψ during the nonlinear stage, indicating that entrainment becomes more important relative to the atomic mixing. In this lower Atwood gas configuration, the layers do not evolve into the homogenous asymptotic mixing state until the reshock rapidly increases the mixed mass and the normalized mixed mass. Again, Ψ reaches a limiting value of $\Psi \approx 0.7 - 0.8$.

To further explore the dependence of the mixed width and mixing efficiency, Fig. 11 shows the transverse average of the total mixed density $\rho_{tot} = 4\rho(Y_1 Y_2 + Y_1 Y_3 + Y_2 Y_3)$. The three-layer high Atwood number case in panel (a) has significantly higher mixed density across a broad region, and the overall mixed width is less than the two-layer case. There is less of a difference for the low A cases in panel (b). This analysis was repeated for data at $t = 15$ ms, well after the reshock for all simulations. The high Atwood number case in panel (c) again has a much greater mixed density across a broad region, when compared with the two-layer control case. However, in contrast to the pre-reshock layer in panel (a), the mixed width is now comparable between the two- and three-layer cases. For the lower Atwood number simulations shown in panel (d), there is little change in mixing between the two- and three-layer cases.

IV. CONCLUSION

In conclusion, RMI in a high Atwood number three-layer system produces a more compact and efficient mixing layer than in a two-layer system. At lower Atwood numbers, the effect of the third layer is minimal. The simulations presented here indicate that overall mixing, as measured by the total mixed mass, is largely unaffected by the presence of an intermediate layer and may even slightly increase. The total mixed mass is dominated by material that is closest to the perturbed interfaces. The presence of a central intermediate layer initially blocks the mixing between the two layers on either side of it.

The mixed width growth is reduced by the central layer. This reduction can be mitigated if both initial interfaces are perturbed. If the two perturbations are in antiphase, dense spikes composed of the central gas can escape the mixing region. In agreement with

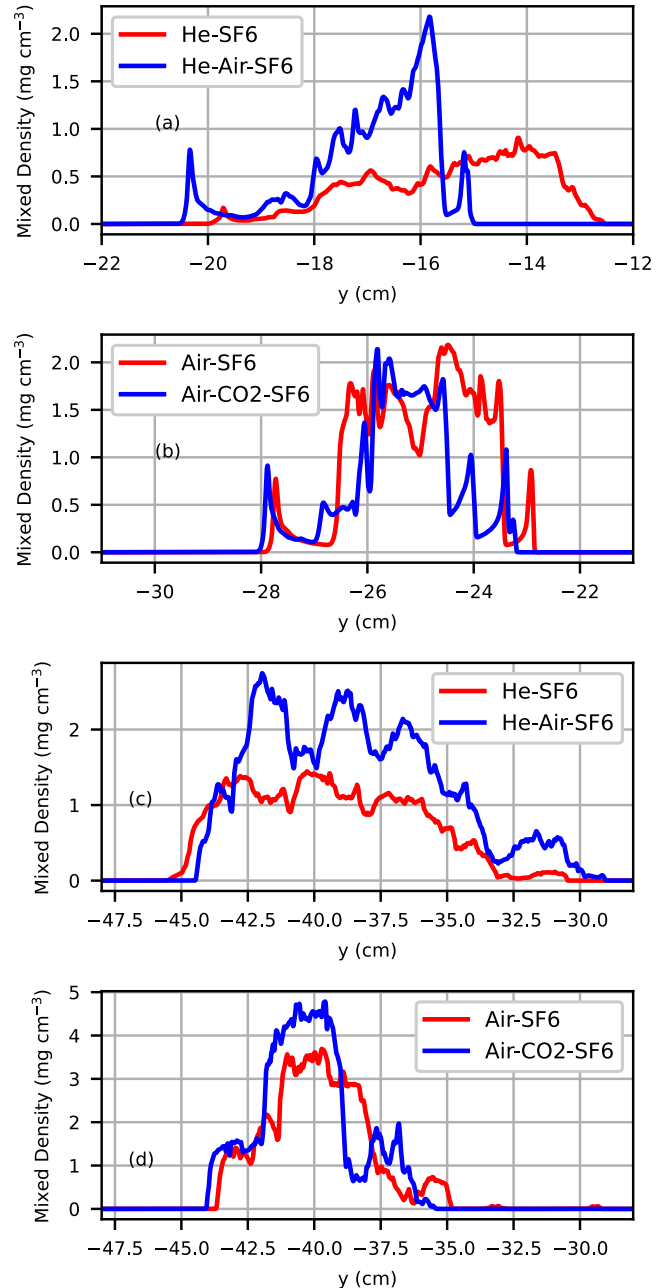


FIG. 11. Transverse average of the total mixed density. Panels (a) and (b) show the high and low Atwood number cases at $ka_0t = 10$, with well-developed RMI before the reshock. Panels (c) and (d) show the high and low Atwood number cases at the end of the simulations at $t = 15$ ms, after the reshock. Red lines show the control two-layer simulation, and blue lines show the three-layer simulation with perturbation only on the lower interface.

prior simulations, a second shock transiting the interface, when it is already in the nonlinear stage, promotes the growth of fine scale structures and increases the mixed width and mixed mass growth rates.

ACKNOWLEDGMENTS

The software used in this work was developed in part by the DOE NNSA and DOE Office of Science-supported Flash Center for Computational Science at the University of Chicago and the University of Rochester.

This work was performed under the auspices of the U.S. Department of Energy by Lawrence Livermore National Laboratory under Contract No. DE-AC52-07NA27344. The work at the University of Arizona was supported by LLNL Subcontract No. B645527.

This document was prepared as an account of work sponsored by an agency of the United States government. Neither the United States government nor Lawrence Livermore National Security, LLC, nor any of their employees makes any warranty, expressed or implied, or assumes any legal liability or responsibility for the accuracy, completeness, or usefulness of any information, apparatus, product, or process disclosed, or represents that its use would not infringe privately owned rights. Reference herein to any specific commercial product, process, or service by trade name, trademark, manufacturer, or otherwise does not necessarily constitute or imply its endorsement, recommendation, or favoring by the United States government or Lawrence Livermore National Security, LLC. The views and opinions of authors expressed herein do not necessarily state or reflect those of the United States government or Lawrence Livermore National Security, LLC, and shall not be used for advertising or product endorsement purposes.

AUTHOR DECLARATIONS

Conflict of Interest

The authors have no conflicts to disclose.

Author Contributions

James D. Sadler: Data curation (equal); Investigation (equal); Writing – original draft (equal); Writing – review & editing (equal). **Philip D. Powell:** Writing – review & editing (equal). **Mark Schalles:** Investigation (equal); Writing – review & editing (equal). **Carlton Martin Louie:** Investigation (equal); Writing – review & editing (equal). **Jeffrey W. Jacobs:** Data curation (equal); Funding acquisition (equal); Investigation (equal); Writing – review & editing (equal). **Ye Zhou:** Conceptualization (equal); Data curation (equal); Funding acquisition (equal); Investigation (equal); Writing – review & editing (equal).

DATA AVAILABILITY

The data that support the findings of this study are available from the corresponding author upon reasonable request.

REFERENCES

- ¹R. D. Richtmyer, “Taylor instability in shock acceleration of compressible fluids,” *Commun. Pure Appl. Math.* **13**, 297–319 (1960).
- ²E. E. Meshkov, “Instability of the interface of two gases accelerated by a shock wave,” *Fluid Dyn.* **4**, 101–104 (1972).
- ³Y. Zhou, “Rayleigh–Taylor and Richtmyer–Meshkov instability induced flow, turbulence, and mixing. I,” *Phys. Rep.* **720–722**, 1–136 (2017).
- ⁴Y. Zhou, “Rayleigh–Taylor and Richtmyer–Meshkov instability induced flow, turbulence, and mixing. II,” *Phys. Rep.* **723–725**, 1–160 (2017).
- ⁵Y. Zhou, R. J. Williams, P. Ramaprabhu, M. Groom, B. Thornber, A. Hillier, W. Mostert, B. Rollin, S. Balachandar, P. D. Powell *et al.*, “Rayleigh–Taylor and Richtmyer–Meshkov instabilities: A journey through scales,” *Physica D* **423**, 132838 (2021).
- ⁶Y. Liang and X. Luo, “Review on hydrodynamic instabilities of a shocked gas layer,” *Sci. China Phys., Mech. Astron.* **66**, 104701 (2023).
- ⁷Y. Zhou, T. T. Clark, D. S. Clark, S. Gail Glendinning, M. Aaron Skinner, C. M. Huntington, O. A. Hurricane, A. M. Dimits, and B. A. Remington, “Turbulent mixing and transition criteria of flows induced by hydrodynamic instabilities,” *Phys. Plasmas* **26**, 080901 (2019).
- ⁸J. Yang, T. Kubota, and E. E. Zukoski, “Applications of shock-induced mixing to supersonic combustion,” *AIAA J.* **31**, 854–862 (1993).
- ⁹J. W. Jacobs, “Shock-induced mixing of a light-gas cylinder,” *J. Fluid Mech.* **234**, 629–649 (1992).
- ¹⁰T. Ma, P. Patel, N. Izumi, P. Springer, M. Key, L. Atherton, L. Benedetti, D. Bradley, D. Callahan, P. Celliers *et al.*, “Onset of hydrodynamic mix in high-velocity, highly compressed inertial confinement fusion implosions,” *Phys. Rev. Lett.* **111**, 085004 (2013).
- ¹¹S. Regan, R. Epstein, B. Hammel, L. Suter, H. Scott, M. Barrios, D. Bradley, D. Callahan, C. Cerjan, G. Collins *et al.*, “Hot-spot mix in ignition-scale inertial confinement fusion targets,” *Phys. Rev. Lett.* **111**, 045001 (2013).
- ¹²A. Pak, L. Divol, C. Weber, L. B. Hopkins, D. Clark, E. Dewald, D. Fittinghoff, V. Geppert-Kleinrath, M. Hohenberger, S. Le Pape *et al.*, “Impact of localized radiative loss on inertial confinement fusion implosions,” *Phys. Rev. Lett.* **124**, 145001 (2020).
- ¹³H. Abu-Shawareb, R. Acree, P. Adams, J. Adams, B. Addis, R. Aden, P. Adrian, B. Afeyan, M. Aggleton, L. Aghaian *et al.*, “Lawson criterion for ignition exceeded in an inertial fusion experiment,” *Phys. Rev. Lett.* **129**, 075001 (2022).
- ¹⁴R. V. Morgan, R. Aure, J. D. Stockero, J. A. Greenough, W. Cabot, O. A. Likhachev, and J. W. Jacobs, “On the late-time growth of the two-dimensional Richtmyer–Meshkov instability in shock tube experiments,” *J. Fluid Mech.* **712**, 354–383 (2012).
- ¹⁵K. O. Mikaelian, “Richtmyer–Meshkov instabilities in stratified fluids,” *Phys. Rev. A* **31**, 410 (1985).
- ¹⁶K. O. Mikaelian, “Rayleigh–Taylor and Richtmyer–Meshkov instabilities in finite-thickness fluid layers,” *Phys. Fluids* **7**, 888–890 (1995).
- ¹⁷K. O. Mikaelian, “Numerical simulations of Richtmyer–Meshkov instabilities in finite-thickness fluid layers,” *Phys. Fluids* **8**, 1269–1292 (1996).
- ¹⁸K. O. Mikaelian, “Rayleigh–Taylor and Richtmyer–Meshkov instabilities and mixing in stratified cylindrical shells,” *Phys. Fluids* **17**, 094105 (2005).
- ¹⁹M. T. Henry de Frahan, P. Movahed, and E. Johnsen, “Numerical simulations of a shock interacting with successive interfaces using the discontinuous Galerkin method: The multilayered Richtmyer–Meshkov and Rayleigh–Taylor instabilities,” *Shock Waves* **25**, 329–345 (2015).
- ²⁰J. W. Jacobs, D. G. Klein, D. L. Jenkins, and R. F. Benjamin, “Instability growth patterns of a shock-accelerated thin fluid layer,” *Phys. Rev. Lett.* **70**, 583 (1993).
- ²¹J. W. Jacobs, D. G. Jenkins, D. L. Klein, and R. F. Benjamin, “Nonlinear growth of the shock-accelerated instability of a thin fluid layer,” *J. Fluid Mech.* **295**, 23–42 (1995).
- ²²Y. Liang, L. Liu, Z. Zhai, J. Ding, T. Si, and X. Luo, “Richtmyer–Meshkov instability on two-dimensional multi-mode interfaces,” *J. Fluid Mech.* **928**, A37 (2021).
- ²³Y. Liang and X. Luo, “On shock-induced heavy-fluid-layer evolution,” *J. Fluid Mech.* **920**, A13 (2021).
- ²⁴Y. Liang and X. Luo, “On shock-induced light-fluid-layer evolution,” *J. Fluid Mech.* **933**, A10 (2022).
- ²⁵Y. Liang and X. Luo, “On shock-induced evolution of a gas layer with two fast/slow interfaces,” *J. Fluid Mech.* **939**, A16 (2022).
- ²⁶Y. Liang and X. Luo, “Hydrodynamic instabilities of two successive slow/fast interfaces induced by a weak shock,” *J. Fluid Mech.* **955**, A40 (2023).
- ²⁷Y. Liang, L. Liu, Z. Zhai, T. Si, and C.-Y. Wen, “Evolution of shock-accelerated heavy gas layer,” *J. Fluid Mech.* **886**, A7 (2020).
- ²⁸Y. Liang and X. Luo, “Shock-induced dual-layer evolution,” *J. Fluid Mech.* **929**, R3 (2021).

- ²⁹J. W. Jacobs and V. V. Krivets, "Experiments on the late-time development of single-mode Richtmyer–Meshkov instability," *Phys. Fluids* **17**, 034105 (2005).
- ³⁰P. Tzeferacos, M. Fatenejad, N. Flocke, C. Graziani, G. Gregori, D. Q. Lamb, D. Lee, J. Meinecke, A. Scopatz, and K. Weide, "Flash MHD simulations of experiments that study shock-generated magnetic fields," *High Energy Density Phys.* **17**, 24–31 (2015).
- ³¹R. V. Morgan, "Experiments on the rarefaction wave driven Rayleigh–Taylor instability," Ph.D. dissertation (The University of Arizona, 2014).
- ³²Y. Zhou, W. H. Cabot, and B. Thornber, "Asymptotic behavior of the mixed mass in Rayleigh–Taylor and Richtmyer–Meshkov instability induced flows," *Phys. Plasmas* **23**, 052712 (2016).
- ³³F. F. Grinstein, L. G. Margolin, and W. J. Rider, *Implicit Large Eddy Simulation* (Cambridge University Press, Cambridge, 2007), Vol. 10.
- ³⁴P. Ramaprabhu, G. Dimonte, P. Woodward, C. Fryer, G. Rockefeller, K. Muthuraman, P.-H. Lin, and J. Jayaraj, "The late-time dynamics of the single-mode Rayleigh–Taylor instability," *Phys. Fluids* **24**, 074107 (2012).
- ³⁵Y. Bin, M. Xiao, Y. Shi, Y. Zhang, and S. Chen, "A new idea to predict reshocked Richtmyer–Meshkov mixing: Constrained large-eddy simulation," *J. Fluid Mech.* **918**, R1 (2021).
- ³⁶J. D. Bender, O. Schilling, K. S. Raman, R. A. Managan, B. J. Olson, S. R. Copeland, C. L. Ellison, D. J. Erskine, C. M. Huntington, B. E. Morgan, S. R. Nagel, S. T. Prisbrey, B. S. Pudliner, P. A. Sterne, C. E. Wehrenberg, and Y. Zhou, "Simulation and flow physics of a shocked and reshocked high-energy-density mixing layer," *J. Fluid Mech.* **915**, A84 (2021).
- ³⁷M. Mohaghar, J. Carter, G. Pathikonda, and D. Ranjan, "The transition to turbulence in shock-driven mixing: Effects of Mach number and initial conditions," *J. Fluid Mech.* **871**, 595 (2019).
- ³⁸M. Mohaghar, J. McFarland, and D. Ranjan, "Three-dimensional simulations of reshocked inclined Richtmyer–Meshkov instability: Effects of initial perturbations," *Phys. Rev. Fluids* **7**, 093902 (2022).
- ³⁹C. D. Noble, J. M. Herzog, A. M. Ames, J. Oakley, D. A. Rothamer, and R. Bonazza, "High speed PLIF study of the Richtmyer–Meshkov instability upon re-shock," *Physica D* **410**, 132519 (2020).
- ⁴⁰C. D. Noble, J. M. Herzog, D. A. Rothamer, A. M. Ames, J. Oakley, and R. Bonazza, "Scalar power spectra and scalar structure function evolution in the Richtmyer–Meshkov instability upon reshock," *J. Fluids Eng.* **142**, 121102 (2020).
- ⁴¹K. O. Mikaelian, "Density gradient stabilization of the Richtmyer–Meshkov instability," *Phys. Fluids A* **3**, 2638–2643 (1991).
- ⁴²A. G. MacPhee, V. A. Smalyuk, O. L. Landen, C. R. Weber, H. F. Robey, E. L. Alfonso, J. Biener, T. Bunn, J. W. Crippen, M. Farrell *et al.*, "Mitigation of x-ray shadow seeding of hydrodynamic instabilities on inertial confinement fusion capsules using a reduced diameter fuel fill-tube," *Phys. Plasmas* **25**, 054505 (2018).
- ⁴³Y. Liang, "The phase effect on the Richtmyer–Meshkov instability of a fluid layer," *Phys. Fluids* **34**, 034106 (2022).
- ⁴⁴B. Thornber and Y. Zhou, "Numerical simulations of the two-dimensional multimode Richtmyer–Meshkov instability," *Phys. Plasmas* **22**, 032309 (2015).
- ⁴⁵B. Thornber and Y. Zhou, "Energy transfer in the Richtmyer–Meshkov instability," *Phys. Rev. E* **86**, 056302 (2012).
- ⁴⁶M. J. Wadas and E. Johnsen, "Interactions of two bubbles along a gaseous interface undergoing the Richtmyer–Meshkov instability in two dimensions," *Physica D* **409**, 132489 (2020).
- ⁴⁷M. J. Wadas, L. H. Khieu, G. S. Cearley, H. J. LeFevre, C. C. Kuranz, and E. Johnsen, "Saturation of vortex rings ejected from shock-accelerated interfaces," *Phys. Rev. Lett.* **130**, 194001 (2023).
- ⁴⁸Y. Zhou, "Unification and extension of the similarity scaling criteria and mixing transition for studying astrophysics using high energy density laboratory experiments or numerical simulations," *Phys. Plasmas* **14**, 082701 (2007).
- ⁴⁹Y. Zhou, "Turbulence theories and statistical closure approaches," *Phys. Rep.* **935**, 1–117 (2021).
- ⁵⁰O. Sadot, L. Erez, U. Alon, D. Oron, L. A. Levin, G. Erez, G. Ben-Dor, and D. Shvarts, "Study of nonlinear evolution of single-mode and two-bubble interaction under Richtmyer–Meshkov instability," *Phys. Rev. Lett.* **80**, 1654 (1998).
- ⁵¹T. Sano, K. Ishigure, and F. Cobos-Campos, "Suppression of the Richtmyer–Meshkov instability due to a density transition layer at the interface," *Phys. Rev. E* **102**, 013203 (2020).
- ⁵²S. R. Nagel, K. S. Raman, C. M. Huntington, S. A. MacLaren, P. Wang, M. A. Barrios, T. Baumann, J. D. Bender, L. R. Benedetti, D. M. Doane *et al.*, "A platform for studying the Rayleigh–Taylor and Richtmyer–Meshkov instabilities in a planar geometry at high energy density at the National Ignition Facility," *Phys. Plasmas* **24**, 072704 (2017).
- ⁵³S. R. Nagel, K. S. Raman, C. M. Huntington, S. A. MacLaren, P. Wang, J. D. Bender, S. T. Prisbrey, and Y. Zhou, "Experiments on the single-mode Richtmyer–Meshkov instability with reshock at high energy densities," *Phys. Plasmas* **29**, 032308 (2022).
- ⁵⁴X. Guo, Z. Cong, T. Si, and X. Luo, "Shock-tube studies of single- and quasi-single-mode perturbation growth in Richtmyer–Meshkov flows with reshock," *J. Fluid Mech.* **941**, A65 (2022).
- ⁵⁵X. Guo, T. Si, Z. Zhai, and X. Luo, "Large-amplitude effects on interface perturbation growth in Richtmyer–Meshkov flows with reshock," *Phys. Fluids* **34**, 082118 (2022).
- ⁵⁶J. Wu, H. Liu, and Z. Xiao, "Refined modelling of the single-mode cylindrical Richtmyer–Meshkov instability," *J. Fluid Mech.* **908**, A9 (2021).
- ⁵⁷M. Latini and O. Schilling, "A comparison of two- and three-dimensional single-mode reshocked Richtmyer–Meshkov instability growth," *Physica D* **401**, 132201 (2020).
- ⁵⁸M. L. Wong, D. Livescu, and S. K. Lele, "High-resolution Navier–Stokes simulations of Richtmyer–Meshkov instability with reshock," *Phys. Rev. Fluids* **4**, 104609 (2019).
- ⁵⁹M. Vetter and B. Sturtevant, "Experiments on the Richtmyer–Meshkov instability of an air/SF₆ interface," *Shock Waves* **4**, 247–252 (1995).